Instrumented nanoindentation and 3D mechanistic modeling of a shale at multiple scales

Kane C. Bennett[1] · Lucas A. Berla[2] · Ronaldo I. Borja[1,*] · William D. Nix?[2]

[1]Department of Civil and Environmental Engineering, Stanford University, Stanford, CA 94305, USA.
[2]Department of Materials Science and Engineering, Stanford University, Stanford, CA 94305, USA

*Corresponding author, E-mail: borja@stanford.edu

Summary. Nanoindentation tests, spanning various length scales ranging from 200 nanometers to 20 micrometers deep, were performed on a sample of organic-rich Woodford shale in both the bedding plane normal and bedding plane parallel directions. Focused ion beam milling (FIB), scanning electron microscopy (SEM), and energy dispersive X-ray spectroscopy (EDX) were used to characterize the shale at the scale of the nanoindentation testing as being comprised predominantly of clay and other silicate minerals suspended in a mixed organic/clay matrix. The nanoindentation tests reveal the mechanical properties of the relatively homogeneous constituent phases as well as those of the highly heterogeneous composite material. Loads on the order of a few milliNewtons produced shallower indents and demonstrated significant elastic response of the constituent materials. Higher loads, reaching as much as a few Newtons, on the other hand, produced deeper indents revealing the elastic-plastic deformation response of the composite matrix. In both cases, significant creep was observed. We use nonlinear finite element modeling utilizing an isotropic critical state theory with creep to capture the indentation responses at the two deformation scales of interest. The simulations reveal the capabilities as well as limitations of an isotropic model in capturing the response of an inherently anisotropic material, thus motivating the development of an anisotropic constitutive model for shale.

Keywords: anisotropy · finite element analysis · heterogeneity · nanoindentation · shale · creep

1 Introduction

Shale is a fine grained sedimentary rock composed primarily of clay, organics, and hard minerals such as quartz, feldspar, and pyrite. It is the most common of sedimentary rocks, having been estimated to form from 44% to 56%

of all sedimentary rocks on earth [7, 27], and is of particular interest with respect to hydrocarbon production as both a source and seal rock [36, 40, 44]. Shale is found to be diverse in composition, leading to its equally diverse thermo-hydro-chemo-mechanical properties. Specifically, the type of clay and other inclusions vary among different shales, as does the presence of other constituents, such as organics, carbonates, smectite, pyrite, and other minerals [7, 24, 27].

The deformation and fracture properties of shale depend on the mechanical properties of its basic constituents. This suggests that a great deal of understanding of the overall macroscopic mechanical properties of shale (as well as other types of rocks) can be gained by studying the small-scale deformation properties of these constituents and how they upscale to the overall behavior of the composite material [4, 5, 14, 43]. Furthermore, the ability to accurately model and predict a shale's stress-strain response is complicated not only by the diversity of its composition, but also by its highly anisotropic and heterogeneous nature. Most researchers agree that anisotropy of shale fabric is associated, in the most general respect, with the parallel alignment of clay particles preferentially oriented in the direction of the bedding plane, which is attributed to deposition, compaction, and/or diagenetic processes [2, 6, 11, 15, 17–19, 25, 27, 28, 30, 31, 37, 39]. Nano-scale to micro-scale heterogeneity is evident because shale is typically comprised of a mixture of micrometer to sub-micrometer sized particles of clay and other minerals, often including organic material (especially when associated with hydrocarbon production) [10, 13, 38, 41]. Mineral inclusions on the scale of micrometers, further, have been shown to produce inhomogeneous deformation within a surrounding clay matrix because of differential stiffness and the resulting effect on the stress field [8, 11].

This paper presents the results of nanoindentation and electron microscopy experiments on a sample of organic rich Woodford shale, carried out for the purpose of qualitatively assessing the heterogeneity, anisotropy, and associated mechanical properties at the nano-to-micro scales. We adopt a deterministic approach to evaluating the mechanical properties of the near micrometer size particles of constituent materials, as well as the highly heterogeneous composite material. Nanoindentation testing, with indents as shallow as 200 nanometers deep, was utilized to measure in situ the deformation behavior of the relatively homogeneous regions comprised of a single material phase, while larger indentations, extending to depths as large as 20 micrometers, provide measurements of their composite deformation behavior. Some rocks are known to creep, particularly shales [21, 34, 35], and so all tests consisted of a peak-load hold period to measure creep. Anisotropy of material properties was evaluated by performing nanoindentation experiments in both the bedding plane normal (BPN) and bedding plane parallel (BPP) directions.

High-resolution imaging has now emerged as a viable means of describing the pore scale characteristics of heterogeneous materials at micro- to nanoscale [9, 12]. In this work, scanning electron microscopy (SEM), focused ion

beam milling (FIB), and energy dispersive X-ray spectroscopy (EDX) were used in conjunction to characterize the heterogeneity and identify the constituent materials (phases) present in the indented regions. The FIB-SEM and EDX nanocharacterization provides a description of the shale sample as being comprised of near micrometer size particles of clay and other silicate minerals embedded in a mixed organic/clay matrix.

Nonlinear finite element modeling (FE) was used to simulate heterogeneous scaled nanoindentation experiments in both the BPN and BPP directions. An isotropic critical state material model with creep was employed for the simulations, which consisted (like the experiments) of large plastic strains. Drucker-Prager/Cap plasticity and consolidation creep material parameters were calibrated to the experiments as a means of evaluating plastic material properties from the nanoindentation measurements. The simulation results reveal the capabilities as well as limitations of an isotropic model in capturing the response of the inherently anisotropic shale at finite plastic strains, thus motivating the development of a finite strain anisotropic material model for shale.

2 Scale and heterogeneity

During the nanocharacterization process, a conceptual model (thought model) of the nano/micro-scale heterogeneity and fabric structure was developed based on the observations. Figure 1 shows schematically the concepts and definitions of scale so adopted with respect to heterogeneity. Three general types of constituent materials (as well as pore space) are recognized: clay particles, other mineral particles, and organic material. The only mineral particles other than clay observed appeared to be quartz and pyrite; notably, no carbonate minerals were observed. This category, therefore, is abbreviated as QFP for quartz, feldspar, and pyrite, which are the most common silicate minerals found in shale [16, 32] and are frequently grouped together in geomechanics applications [22, 35] because they have similar material properties. Although the choice of these three broad categories of constituent materials may seem nebulous from a geochemistry point of view, they are fitting for the mechanistic modeling point of view adopted here because they correspond to three categories encompassing the full range of constituent material stiffness: compliant (organic), medium stiffness (clay), and stiff (QFP).

The FIB-SEM imaging revealed that the shale was comprised predominantly of near micrometer size particles of these three material types; however, it was deemed necessary to define a fourth material category: a composite of two materials, the organic/clay matrix (O/C matrix). The description of the organic/clay matrix emerged from the observation that the mineral particles and pockets of organic material did not form a supporting skeleton with intergranular contacts, such as has been observed by some researchers [35, 38], but rather were embedded in a supporting matrix composed of varying sizes of clay

plate shaped particles mixed with organic material, which has also been observed in organic rich shales by other researchers [33, 41]. These plate-shaped particles of clay (mixed with organics) were observed to range down to sizes near the resolution of the SEM, i.e., with thicknesses near one nanometer. Figures 2 and 3 show the observed mineralogy and the supporting organic/clay matrix with various size plate-shaped clay particles evident.

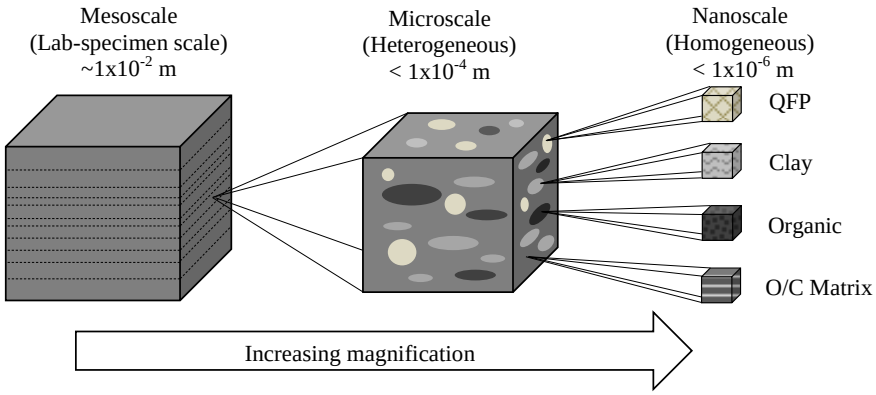

Fig. 1: Concepts and definitions of scale with respect to heterogeneity.

3 Experimental methods

3.1 Sample preparation

A sample of an organic rich Woodford shale was obtained from a hydrocarbon reservoir exploratory wellbore. The location and depth of the sampling was not disclosed for proprietary reasons. The samples were prepared by mechanical polishing at the Sensitive High Resolution Ion Micro Probe Reverse Geometry (SHRIMP) lab at Stanford University. Polishing consisted of first setting the sample in epoxy and then hand grinding two parallel faces with 400, 600, then 1500 grit emery cloth. A Struers Labopol-5 polishing machine was then used with 6 micrometer (µm) diamond suspension polishing fluid, followed by 1 µm diamond suspension polishing fluid, and finally 40 nanometer (nm) colloidal silica suspension.

3.2 FIB-SEM and EDX methods

Focused ion beam (FIB) milling and scanning electron microscopy (SEM) were used in conjunction (FIB-SEM) for nanocharacterization of pre- and post-indented shale specimens. The FIB-SEM nanocharacterization was performed with an FEI Helios NanoLab 600i DualBeam FIB/SEM at the Stanford Nanocharacterization Laboratory. Figure 2 shows a backscatter electron (BSE) image of a BPP shale sample. Pyrite minerals are easily distinguished by their relative brightness due to the iron they contain. Silicate minerals (particularly quartz) and clay can be more difficult to distinguish in the BSE image due to similar contrast, so they must be distinguished by shape and with aid of EDX spectroscopy. The organic matter appears very dark because of the relatively low atomic weight of the carbon it contains. Figure 3 shows an image of a FIB milled trench cut into the shale surface. The thin coating of gold and thicker coating of carbon visible at the top of the figure are deposited to provide surface conductivity and protection from the FIB, respectively.

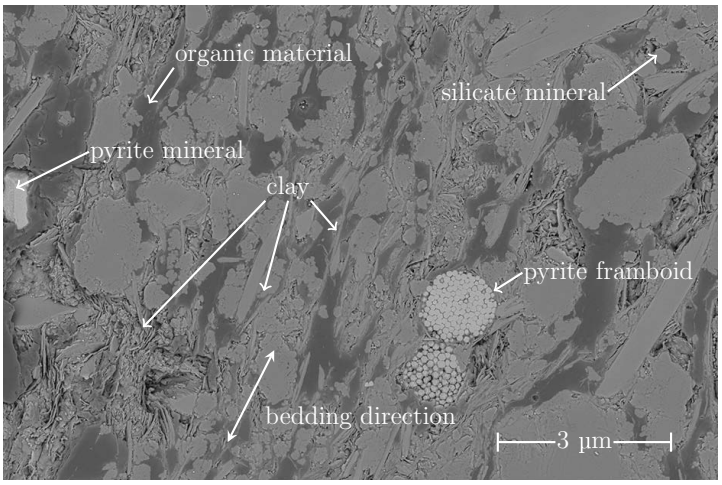

Fig. 2: SEM image of polished shale sample surface.

Energy dispersive X-ray spectroscopy (EDX) was used to identify the constituent materials present in the shale specimen. The work was performed at the Stanford Nanocharacterization Laboratory with an FEI Strata 235DB dual-beam FIB/SEM, which has element mapping and EDX microchemical analysis capability. Figure 4 shows an example EDX spectrograph of a clay particle. The spectrograph was used as an aid to identify specific shale constituents, which must otherwise be identified by their shape and contrast as detected by backscatter electron (BSE) emission.

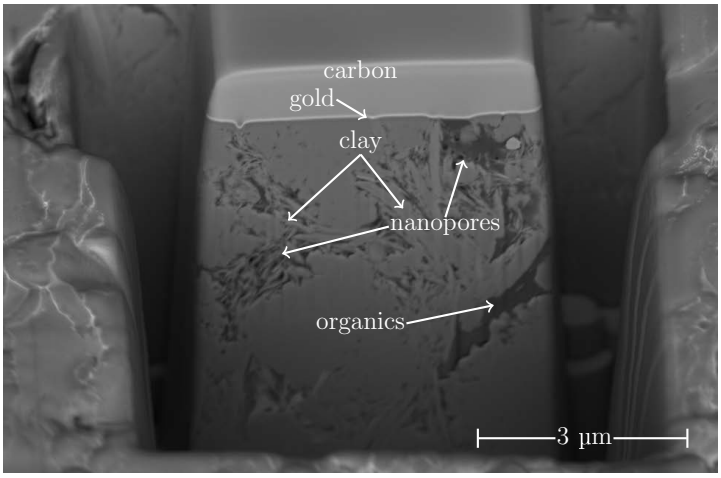

Fig. 3: SEM image of FIB milled trench into surface exposing a face for serial sectioning.

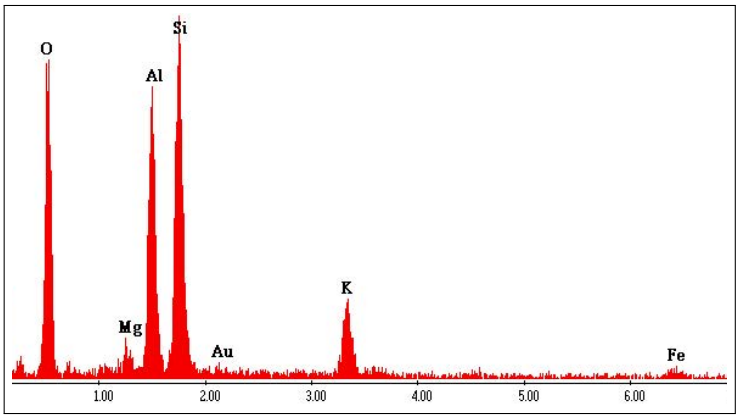

Fig. 4: Spectrograph from EDX analysis of clay particle.

3.3 Nanoindentation methods

Nanoindentation was performed with a diamond Berkovich indenter tip on an Agilent Technologies Nanoindenter XP with high load capabilities. The indentation apparatus has a displacement resolution of 0.01 nm and a load resolution of 100 nN during standard loading. Nanoindentation experiments have been performed to various indentation depths, engaging the various length scales of the sample heterogeneity: 200 nm, 1 µm, 3 µm, 5 µm, and ∼20 µm deep. Indentations have been made into two different specimens cut from the same sample: bedding plane parallel (BPP) and bedding plane normal (BPN)

oriented shale specimens. A total of 349 individual indentations were made. All were performed load (P) controlled, and displacement of the tip into the surface h was measured. The deepest indents (∼20 µm) were performed by loading at a constant loading rate for 120 s to a specified maximum load ($P_{\max}$), holding at the peak load for 180 s, and then unloading. The rest of the indents were made by loading to a specified indentation depth (h_{load}), with indenter loading done so as to maintain a constant indentation strain rate $\dot{P}/P$. A target effective strain rate of $\dot{P}/P = 0.05\,\text{s}^{-1}$ was chosen. In all cases, the peak indentation load was held for some time to measure the creep behavior of the indented material. The peak hold time t_{creep} was 60 seconds for most tests, but some tests were held at peak load for as much as 20 minutes as extended creep tests.

The nanoindentation experiments were performed in large grid patterns with known indent spacing so that individual indents could later be identified by SEM. Imaging the residual impressions with the SEM made possible identification of indents that fell on locally rough areas; data corresponding to such indents was discarded. Furthermore, with SEM, indents that were found to fall within a relatively homogeneous region comprised of a single constituent material were identified, as will be discussed in the presentation of the results in Section 4.2.

The material properties extracted from the nanoindentation measurements include the reduced modulus E_r, hardness H, and the normalized plastic work ratio W_p^*. The reduced modulus E_r is calculated from the initial slope of the $P - h$ unloading curve according to

$$E_r = \frac{1}{2\alpha}\sqrt{\frac{\pi}{A_c}}\frac{dP}{dh}, \tag{1}$$

where the projected contact area A_c is calculated from the calibrated tip shape function, and α is a constant related to the geometry of the indenter, taken as $\alpha = 1.034$. With knowledge of the reduced modulus and Poisson's ratio ν, Young's modulus of the indented material can be found from

$$\frac{1}{E_r} = \frac{1-\nu^2}{E} + \frac{1-\nu_i^2}{E_i}, \tag{2}$$

where E_i and ν_i are Young's modulus and Poisson's ratio, respectively, of the diamond indenter. To avoid the necessity of assuming ν, we report the effective modulus E_s, defined as

$$E_s := \frac{E}{1-\nu^2}. \tag{3}$$

The hardness H is calculated as the ratio of the peak load to the projected contact area at peak load,

$$H = \frac{P_{\max}}{A_c}. \tag{4}$$

The normalized plastic work ratio W_p^* is calculated from the areas under the loading and unloading portions of the $P-h$ curve, which correspond to the total work W_t and elastic work W_e, respectively. The total work is assumed to be additively composed of elastic and plastic parts, i.e., $W_t = W_p + W_e$, allowing for the expression of the normalized plastic work to be defined as

$$W_p^* := \frac{W_p}{W_t} = 1 - \frac{W_e}{W_t}. \tag{5}$$

4 Experimental results

4.1 FIB-SEM and EDX results

FIB-SEM and EDX nanocharacterization has led to the development of the underlying thought model of heterogeneity and scales discussed in Section 2. The sample was observed to have a relatively high organic content compared to images reviewed in the literature. Our FIB-SEM characterization of the shale sample provides a *description of the shale at this scale as being comprised of near micrometer sized particles of clay and other silicate minerals embedded in a mixed organic/clay matrix*. Nearly everywhere that organic material is observed, clay platelets are found to be interspersed within, as seen in Figures 2 and 3.

The SEM imaging was also instrumental in evaluating the local surface roughness and constituent materials present at the location of the indentations, as is discussed next in the Section 4.2. Figure 5 shows a backscatter electron (BSE) image of the residual impression left by a 3 µm deep BPP indentation into a highly heterogeneous region.

4.2 Nanoindentation results

Each indentation locus from the full set of BPN and BPP nanoindentation results were examined individually by SEM in order to 1) disregard indents that fell on a locally rough surface, and 2) identify indents which fell on relatively homogeneous regions comprised of a single constituent material. It is well known that surface roughness can lead to inaccuracy in indentation measurements [26], and, therefore, it is important to ensure that indentation measurements are performed on an adequately smooth surface. This can prove to be a challenge in the case of shale because of its highly heterogeneous nature at the scale of the nanoindentation testing. It was thus decided that each indentation locus would be examined individually by SEM so that the local surface roughness could be evaluated and those that fell on locally rough surfaces discarded. Examination of the surface engaged by each indentation measurement, furthermore, allowed the material comprising the surface at the location of the indent to be evaluated. Because the heterogeneity at the scale

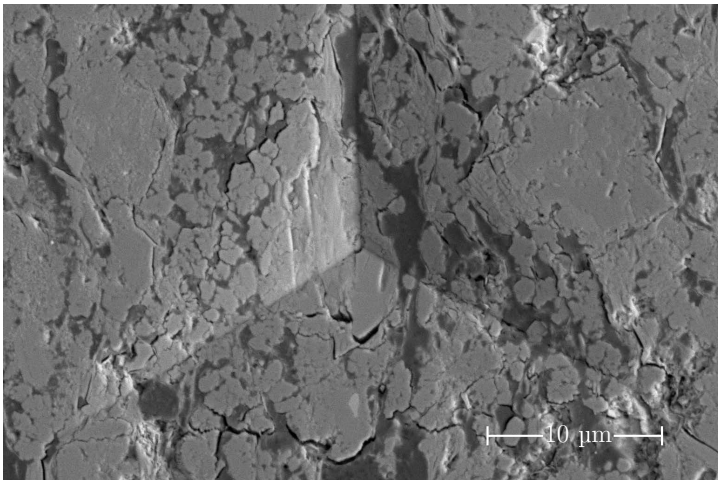

Fig. 5: Backscatter electron (BSE) image of post indented region of 3µm deep BPP test showing residual impression within highly heterogeneous material.

of the indents consisted of approximately micrometer size particles of clay and silicate mineral grains suspended in a mixed organic/clay matrix, some of the 200 nm deep indentations were found to engage, at least predominantly, a single material phase. The 1 µm deep indentations were found to be generally too large to fall within a single homogeneous phase; however, some of them were found to fall *between* particles, i.e. in regions comprised of only the organic/clay matrix, and some were found to fall in relatively large pockets of organic material. Indentations 3 µm deep and larger were found to fall in heterogeneous regions, with the exception of two of the 3 µm deep indentations which engaged (relatively) large pockets of organic material.

The 200 nm deep indents are thus divided into three groups: those that fell on particles of clay, those that fell on other silicate mineral particles (abbreviated QFP), and those that fell on regions of organic matter. It should be noted that while some of the 200 nm deep indentations were found to fall on predominantly a single phase, surrounding constituent materials and the supporting matrix likely influence to some extent the indentation measurements. Figure 6 presents nanoindentation load-displacement curves obtained from 200 nm deep indents, with the results grouped as described above. Table 1 shows the subsequently extracted mechanical properties. The 1 µm deep indentations provide measurements of the mechanical properties of the O/C matrix, reported in Table 2.

The indentations to depths of 3 µm were found to fall on heterogeneous regions, with the notable exception of two of the 3 µm deep indentations which fell on relatively large pockets of organic matter, one from each of the BPN

and BPP data sets. The 5 µm deep indentations all engaged heterogeneous regions, as did the high-load (∼20 µm) indentations. Figure 7 shows how the 5 µm deep indentations varied relatively little, being representative of the deformation behavior of the composite (heterogeneous) material. The extracted mechanical properties for the heterogeneous material at these scales are presented in Table 3, and extracted mechanical properties of the organic material are presented in Table 4.

Table 1: Measured mechanical properties of each of the constituent materials as measured by 200 nm deep indentation tests in both BPN and BPP orientations.

		BPN			BPP		
		Mean	SD	COV (%)	Mean	SD	COV (%)
QFP	E_s (GPa)	32.750	7.287	22.25	38.114	7.029	18.43
	H (GPa)	4.515	0.713	15.79	4.815	1.502	31.19
	W_p^*(%)	50.59	1.84	3.64	55.92	4.73	8.46
Clay	E_s (GPa)	20.373	2.927	14.37	25.865	5.692	22.01
	H (GPa)	1.801	0.242	13.42	1.592	0.332	20.83
	W_p^*(%)	61.02	2.24	3.67	68.93	5.45	7.91
Organic	E_s (GPa)	8.780	3.094	35.24	6.503	-	-
	H (GPa)	0.449	0.155	34.60	0.278	-	-
	W_p^*(%)	62.32	24.52	39.35	74.61	-	-

Table 2: Measured mechanical properties of organic/clay matrix as measured by 1 µm deep indentation tests in both BPN and BPP orientations.

		BPN			BPP		
		Mean	SD	COV (%)	Mean	SD	COV (%)
O/C Matrix	E_s (GPa)	12.392	1.498	12.09	18.545	1.975	10.65
	H (GPa)	0.604	0.075	12.38	0.592	0.088	14.81
	W_p^*(%)	67.98	2.78	4.09	74.69	3.24	4.34

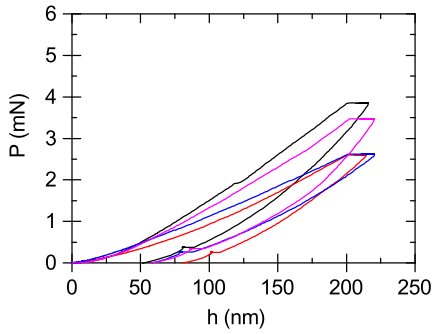

(a) BPN indentations into QFP-silicate mineral grains.

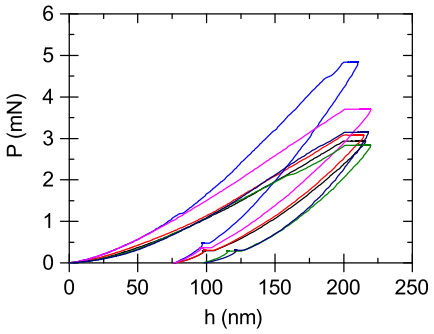

(b) BPP indentations into QFP-silicate mineral grains.

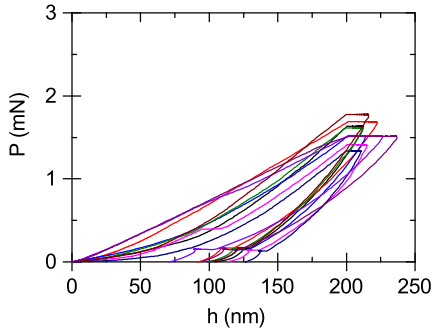

(c) BPN indentations into clay particles.

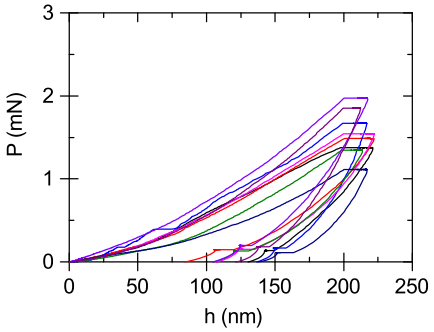

(d) BPP indentations into clay particles.

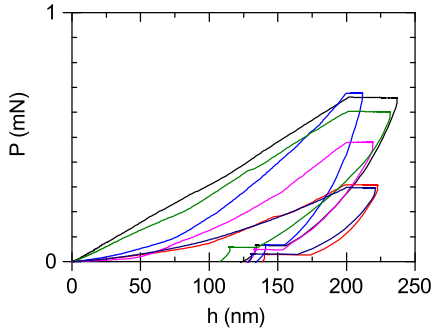

(e) BPN indentations into organic material.

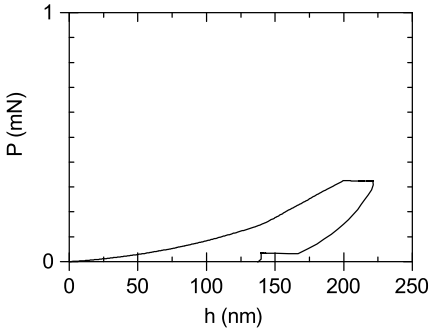

(f) BPP indentation that fell on pocket of organic material.

Fig. 6: BPN (left) and BPP (right) load-versus-displacement curves for 200 nm deep indentations grouped by the constituent material on which they fell.

Table 3: Measured mechanical properties of heterogeneous shale measured at various length scales in both BPN and BPP orientations.

Depth		BPN			BPP		
		Mean	SD	COV (%)	Mean	SD	COV (%)
3 µm	E_s (GPa)	12.981	0.554	4.27	17.187	1.174	6.83
	H (GPa)	0.480	0.041	8.48	0.556	0.073	13.20
	W_p^*(%)	71.75	1.64	2.29	75.53	19.54	25.87
5 µm	E_s (GPa)	11.792	0.622	5.28	15.174	0.763	5.02
	H (GPa)	0.406	0.020	4.99	0.452	0.038	8.52
	W_p^*(%)	72.95	1.04	1.43	76.51	1.51	1.97
∼20 µm	E_s (GPa)	12.519	1.085	8.67	13.109	1.780	13.58
	H (GPa)	0.352	0.020	5.80	0.408	0.029	7.06
	W_p^*(%)	79.09	1.28	1.62	76.96	1.21	1.57

Table 4: Measured mechanical properties of organic material measured at various length scales and in both BPN and BPP orientations.

Depth		BPN			BPP		
		Mean	SD	COV (%)	Mean	SD	COV (%)
1 µm	E_s (GPa)	10.668	1.124	10.53	9.511	1.573	16.53
	H (GPa)	0.295	0.041	14.14	0.299	0.097	32.44
	W_p^*(%)	78.07	2.81	3.60	72.52	2.28	3.14
3 µm	E_s (GPa)	6.173	-	-	10.042	-	-
	H (GPa)	0.282	-	-	0.317	-	-
	W_p^*(%)	60.42	-	-	70.35	-	-

5 FE model

5.1 Model development

Figure 8 shows the meshed nanoindentation model with a Berkovich indenter tip, consisting of a total of 10,161 elements. The nonlinear FE modeling was done in Abaqus/standard with implicit integration. The shale was modeled with linear hexahedral elements using reduced integration, and the Berkovich tip was modeled as a rigid body (its motion governed by a reference node at its tip) with a mixture of linear quadrilateral and linear triangular elements. The contact between shale and the indenter was modeled as surface-to-surface frictionless contact with a finite-sliding Lagrange multiplier formulation. The boundary conditions (BC's) of the shale were prescribed as fully fixed (essen-

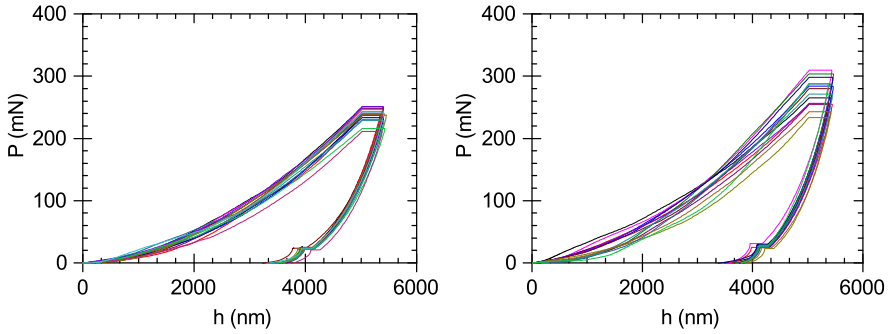

(a) BPN heterogeneous (b) BPP heterogeneous

Fig. 7: BPN (Left) and BPP (Right) 5 µm deep indentations into heterogeneous regions showing repeatability of measurements, indicating that they are representative of the composite material response.

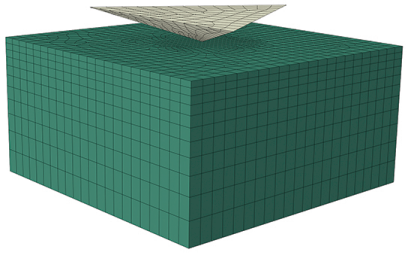

Fig. 8: Meshed model of shale nanoindentation with a Berkovich indenter tip.

tial BC's) at the base, laterally fixed at the sides, and fully free (natural BC's) at the top surface where the indenter made contact.

Both the BPN and BPP 3 µm deep heterogeneous indentations were simulated. Imitating the nanoindentation experiments, the simulations were performed to a specified indentation depth h by controlling the applied load P so as to maintain a constant indentation rate (Section 3.3). That is, during simulated loading, the load was made to evolve over time according to

$$P(t) = P_0 e^{kt}. \tag{6}$$

The loading parameters P_0 and k were determined from the experiments to be 0.022 mN and 0.0156 s^{-1}, respectively. Once the target depth was reached, the load was held constant for 60 seconds, and then the indenter was unloaded (linearly in time) to $P = 0$ over 20 seconds.

Because the nanoindentation experiments show significant creep in addition to plastic deformation, a viscoplastic creep material model has been

pursued. To this end, isotropic linear elasticity and a Modified Drucker-Prager/Cap plasticity with consolidation hardening and creep was chosen. Modified Drucker-Prager/Cap plasticity is based on the well known Drucker-Prager plasticity yield criterion for granular materials with the addition of a cap bounding the yield surface in the direction of the mean normal stress p (along the hydrostatic axis). A detailed description of the material model can be found in [1], and is not repeated here; however, a general description and definition of the material parameters is provided in what follows.

Denoting tensors in boldface, we note the use of $\mathbf{1}$ for the second order identity tensor and $\boldsymbol{\sigma}$ for the Cauchy stress tensor. The inner (scalar) product of two tensors is signified by the double dot, e.g. $\boldsymbol{A} : \boldsymbol{B} = \mathrm{tr}[\boldsymbol{A}^T \boldsymbol{B}]$, where we have denoted the matrix transpose with the superscript T and the matrix trace operator $\mathrm{tr}[\bullet]$. The deviatoric stress $\boldsymbol{S}$ is given by $\boldsymbol{S} := \boldsymbol{\sigma} - 1/3\,\mathrm{tr}\,[\boldsymbol{\sigma}]\mathbf{1}$.

The yield surface is defined in $p - q$ space, where the mean normal stress p and Mises equivalent stress q are defined as

$$p := \frac{1}{3}\,\mathrm{tr}[\boldsymbol{\sigma}], \quad q := \sqrt{\frac{3}{2}\boldsymbol{S} : \boldsymbol{S}}. \tag{7}$$

The cohesion d and the friction angle β define the cohesive bounding surface (in the direction of q). The creep formulation is restricted to an associated flow rule (no dependence on the third stress invariant). The initial intersection of the cap with the hydrostatic axis $p_{b(1)}$ is specified along with a second hydrostatic yield stress point $p_{b(2)}$ and a corresponding amount of plastic volumetric strain ε_v^{pl}, which together define linear cap hardening.

The total strain $\boldsymbol{\varepsilon}$ is assumed to be additively composed of elastic and inelastic (plastic) parts, with the inelastic strain, furthermore, composed of the time-independent part $\boldsymbol{\varepsilon}^{pl}$ and the time-dependent (creep) part $\boldsymbol{\varepsilon}^{cr}$, such that

$$\boldsymbol{\varepsilon} = \boldsymbol{\varepsilon}^{el} + \boldsymbol{\varepsilon}^{pl} + \boldsymbol{\varepsilon}^{cr}. \tag{8}$$

The creep is defined with respect to the mean normal stress p (consolidation creep), where the effective creep pressure $\bar{p}^{cr}$ describes a pressure within the yield surface but greater than a threshold creeping pressure (related to the yield surface cap position). The creep strain increment $\Delta\boldsymbol{\varepsilon}^{cr}$ is proportional to the equivalent creep strain $\bar{\varepsilon}_c^{cr}$, which is determined from a uniaxial consolidation law. A time (t) dependent uniaxial creep law was chosen, given by

$$\dot{\bar{\varepsilon}}_c^{cr} = A(\bar{p}^{cr})^n t^m, \tag{9}$$

where A, n, and m are material parameters.

5.2 Simulation results

Simulations and material model calibrations were performed separately for the bedding plane normal (BPN) and bedding plane perpendicular (BPP)

Table 5: Calibrated material parameters for BPN simulation.

Drucker-Prager Plastic				Cap Hardening		Creep Consolidation		
E (GPa)	ν	d (MPa)	β	$p_{b(1\&2)}$ (MPa)	ε_v^{pl}	A ($\mathrm{Pa^n s^m}$)	n	m
7.70	0.3	114	36°	395 1625	0 0.2	1E-18	2.10	-0.5

simulations. Initial trial material parameters were estimated from the nanoindentation results (Section 4.2) along with consideration of other published laboratory testing results [3, 23, 29, 35]; however, the final material model parameters were determined by calibrating the simulations to the nanoindentation experiments.

Average $P-h$ measurement curves were estimated for both the BPN and BPP 3 µm data sets, and are presented alongside the simulation results in Figure 9. The average measurement curves were established as having the mean peak load $\bar{P}_{\max}$ and amount of creep during the peak load hold period $\bar{\Delta}h_{\mathrm{creep}}$. The average loading and unloading curves were determined separately by least squares polynomial regression.

Figure 9 presents the results of the calibration alongside the laboratory measurements. The calibrated material parameters are presented in Tables 5 and 6 for the BPN and BPP simulations, respectively.

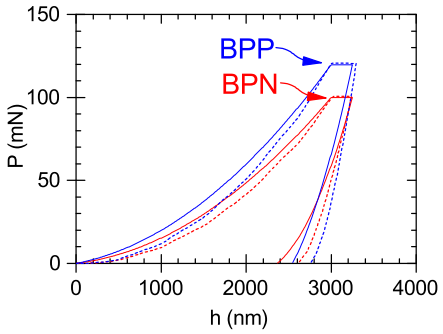

Fig. 9: BPN and BPP simulation results compared with average of corresponding laboratory measurements. Measurements are shown with solid lines and simulations with dashed lines.

Table 6: Calibrated material parameters for BPP simulation.

Drucker-Prager Plastic				Cap Hardening		Creep Consolidation		
E (GPa)	ν	d (MPa)	β	$p_{b(1\&2)}$ (MPa)	ε_v^{pl}	A ($\mathrm{Pa^n s^m}$)	n	m
10.2	0.3	123	40°	430 1640	0 0.2	1E-18	2.10	-0.5

6 Conclusions

Nanoindentation tests as shallow as 200 nm have provided in situ mechanical property measurements of the constituent materials comprising a highly heterogeneous sample of Woodford shale, whereas indentations ranging to depths of up to ∼20 µm have provided measurements of their composite mechanical properties. Nanoindentation testing was performed in both the bedding plane normal (BPN) and bedding plane perpendicular (BPP) directions to evaluate material anisotropy. FIB-SEM imaging provided verification that indents at all length scales fell on sufficiently smooth regions and, along with EDX spectroscopy, provided for identification of the material phases on which the smallest indents fell.

The FIB-SEM imaging further enabled the development of a conceptual model describing the scale with respect to material heterogeneity for the organic-rich shale specimen: the specimen was found to be best described as being comprised of near micrometer sized particles of clay and other silicate minerals embedded in a mixed organic/clay matrix. Together with the nanoindentation testing, the FIB-SEM imaging identified a separation of scale at approximately 1 µm occurring between relatively homogeneous regions comprised of a single material phase and highly heterogeneous regions representing the composite material. The 200 nm deep indentations were observed to be predominantly representative of the constituent phases on which they fell, whereas indentations ranging from depths of 3 µm to ∼20 µm were shown to be representative of the composite (heterogeneous) material response. Indentations to depths of 1 µm measured the mechanical properties of the organic/clay matrix.

A FE model of the nanoindentation experiments was developed and implemented with Drucker-Prager/Cap plasticity and consolidation creep. Plastic material parameters were calibrated to the 3 µm deep indentation measurements which represent the stress-strain behavior of the heterogeneous shale. The calibrated simulations provide a means of extracting plastic material parameters from the nanoindentation experiments. The different material properties calibrated for BPN and BPP indentations provide a measure of the material anisotropy, and also motivate the development of a finite strain anisotropic material model for shale.

Acknowledgments

This work is supported by the US Department of Energy under Grant No. DE-FG02-03ER15454 to Stanford University. L.A.B. and W.D.N. gratefully acknowledge support from the Office of Science, Office of Basic Energy Sciences, of the U.S. Department of Energy under Contract No. DE-FG02-04ER46163. The first author is grateful for a National Defense Science and Engineering (NDSEG) Graduate Fellowship. The authors wish to thank Dr. Younane N. Abousleiman of the University of Oklahoma for providing samples of Woodford shale, and Dr. Cindy Ross of Stanford's Department of Energy Resource Engineering for assistance in preparing the samples.

References

[1] Abaqus (2011). Abaqus documentation. Technical report, Dassault Systems, Providence, RI, USA.

[2] Abousleiman YN, Hoang SK, Liu C (2014) Anisotropic porothermoelastic solution and hydro-thermal effects on fracture width in hydraulic fracturing. Int J Numer Anal Meth Geomech 38(5):493–517

[3] Abousleiman, Y., M. Tran, S. Hoang, C. Bobko, A. Ortega, & F. Ulm (2007). Geomechanics field characterization of woodford shale: The next gas play. In *Proceedings - SPE Annual Technical Conference and Exhibition*, Anaheim, CA, USA, pp. 2127–2140.

[4] Arson C, Pereira JM (2013) Influence of damage on pore size distribution and permeability of rocks. Int J Numer Anal Meth Geomech 37(8):810–831

[5] Barthélémy JF, Souque C, Daniel JM (2013) Nonlinear homogenization approach to the friction coefficient of a quartz-clay fault gouge. Int J Numer Anal Meth Geomech 37(13):1948–1968

[6] Bennett R, O'Brien N, Hulbert M (1991) Determinants of clay and shale microfabric signatures: Processes and mechanisms. In: Bennett R, Bryant W, Hulbert M (eds) Microstructure of Fine-Grained Sediments: From Mud to Shale, Springer-Verlag, New York, N.Y.

[7] Boggs S (2009) Petrology of Sedimentary Rocks. Cambridge University Press, Cambridge, GBR

[8] Bornert M, Vales F, Gharbi H, Minh D (2010) Multiscale full-field strain measurements for micromechanical investigations of the hydromechanical behavior of clayey rocks. Strain 46:33–46

[9] Brooks Z, Ulm FJ, Einstein HH (2013) Environmental scanning electron microscopy (ESEM) and nanoindentation investigation of the crack tip process zone in marble. Acta Geotech 8(3):223–245

[10] Curtis M, Ambrose R, CH S, Rai C (2011) Transmission and scanning electron microscopy investigation of pore connectivity of gas shales on

the nanoscale. In: SPE North American Unconventional Gas Conference and Exhibition, Woodlands, TX

[11] Day-Stirrat R, Dutton S, Millken K, Loucks R, Aplin A, Hillier S, van der Pluijm B (2010) Fabric anisotropy induced by primary depositional variations in the silt: clay ratio in two fine-grained slope fan complexes: Texas gulf coast and northern north sea. Sediment Geol 226:42–53

[12] Deirieh A, Ortega JA, Ulm FJ, Abousleiman Y (2012) Nanochemomechanical assessment of shale: a coupled WDS-indentation analysis. Acta Geotech 7(4):271–295

[13] Dewers T, Heath J, Ewy R, Duranti L (2012) Three-dimensional pore networks and transport properties of a shale gas formation determined from focused ion beam serial imaging. Int J Oil, Gas and Coal Technology 5(2-3):229–248

[14] Foster CD, Mohammad Nejad T (2013) Embedded discontinuity finite element modeling of fluid flow in fractured porous media. Acta Geotech 8(1):49–57

[15] He Z, Caratini G, Dormicux L, Kondo D (2013) Homogenization of anisotropic elastoplastic behaviors of a porous polycrystal with interface effects. Int J Numer Anal Meth Geomech 37(18):3213–3236

[16] Hiller S (2006) Appendix a. mineralogical and chemical data. Geological Society, London, Engineering Geology Special Publications 21:449–459

[17] Hu DW, Zhou H, Shao JF (2013) An anisotropic damage-plasticity model for saturated quasi-brittle materials. Int J Numer Anal Meth Geomech 37(12):1691–1710

[18] Hu DW, Zhang F, Shao JF (2014) Experimental study of poromechanical behavior of saturated claystone under triaxial compression. Acta Geotech 9(2):207–214

[19] Ingram R (1953) Fissility of mudrocks. Geol Soc Am Bull 64:869–878

[20] ISO-14577 (2002) Metallic materials - instrumented indentation test for hardness and materials parameters

[21] Karim MR, Oka F, Krabbenhoft K, Leroueil S, Kimoto S (2013) Simulation of long-term consolidation behavior of soft sensitive clay using an elasto-viscoplastic constitutive model. Int J Numer Anal Meth Geomech 37(16):2801–2824

[22] Kohli A, Zoback M (1983) Frictional properties of shale reservoir rocks. J Geophys Res-Sol Ea 118:1–17

[23] Kumar, V. (2012). *Geomechanical Characterization of Shale Using Nano-Indentation*. Ph. D. thesis, OK University.

[24] Lee S, Hyder L, Alley P (1991) Microstructural and mineralogical characterization of selected shales in support of nuclear waste repository studies. In: Bennett R, Bryant W, Hulbert M (eds) Microstructure of Fine-Grained Sediments: From Mud to Shale, Springer-Verlag, New York, NY

[25] Lonardelli I, Wenk H, Ren Y (2007) Preferred orientation and elastic anisotropy in shales. Geophysics 72(2):D33–D40

[26] Lucas B, Oliver W, Swindeman J (1998) The dynamics of frequency-specific, depth-sensing indentation testing. Mat Res Soc Symp Proc 522:3–14

[27] Pettijohn F (1975) Sedimentary Rocks, 3rd edn. Harper and Row Publishers, New York, NY

[28] Pietruszczak S, Guo P (2013) Description of deformation process in inherently anisotropic granular materials. Int J Numer Anal Meth Geomech 37(5):478–490

[29] Powell, J., W. Take, G. Siemens, & V. Remenda (2012). Time-dependent behavior of the bearpaw shale on oedometric loading and unloading. *Can. Geotech. J.* 49, 427–441

[30] Salager S, Francois B, Nuth M, Laloui L (2013) Constitutive analysis of the mechanical anisotropy of Opalinus Clay. Acta Geotech 8(2):137–154

[31] Schaedlich B, Schweiger HF (2013) A multilaminate constitutive model accounting for anisotropic small strain stiffness. Int J Numer Anal Meth Geomech 37(10):1337–1362

[32] Shaw D, Weaver C (1965) The mineralogical composition of shales. J Sed Pet 35(1):213–222

[33] Sondergeld C, Ambrose R, Rai C, Moncrieff J (2010) Micro-structural studies of gas shales. In: Proceedings of SPE Unconventional Gas Conference, Pittsburgh, PA, USA

[34] Nedjar B, Le Roy R (2013) An approach to the modeling of viscoelastic damage. Application to the long-term creep of gypsum rock materials. Int J Numer Anal Meth Geomech 37(9):1066–1078

[35] Sone H, Zoback M (2013) Mechanical properties of shale-gas reservoir rocks - part 2: Ductile creep, brittle strength, and their relation to the elastic modulus. Can Geotech J 78:D393–D402

[36] Tian H, Xu T, Wang F, Patil VV, Sun Y, Yue G (2014) A numerical study of mineral alteration and self-sealing efficiency of a caprock for CO2 geological storage. Acta Geotech 9(1):87–100

[37] Tran HTT, Wong H, Dubujet P, Doanh T (2014) Simulating the effects of induced anisotropy on liquefaction potential using a new constitutive model. Int J Numer Anal Meth Geomech 38(10):1013–1035

[38] Ulm F, Aboussleiman Y (2006) The nanogranular nature of shale. Acta Geotechnica 1:77–88

[39] Valcke S, Casey M, Lloyd G, Kendall J, Fisher Q (2006) Lattice preferred orientation and seismic anisotropy in sedimentary rocks. Geopys J Int 166:652–666

[40] Vallin V, Pereira JM, Fabbri A, Wong H (2013) Numerical modelling of the hydro-chemo-mechanical behaviour of geomaterials in the context of CO2 injection. Int J Numer Anal Meth Geomech 37(17):3052–3069

[41] Vernik L, Nur A (1992) Ultrasonic velocity and anisotropy of hydrocarbon source rocks. Geophys 57(5):727–735

[42] Vitone C, Viggiani G, Cotecchia F, Hall SA (2013) Localized deformation in intensely fissured clays studied by 2D digital image correlation. Acta Geotech 8(3):247–263

[43] White JA (2014) Anisotropic damage of rock joints during cyclic loading: constitutive framework and numerical integration. Int J Numer Anal Meth Geomech 38(10):1036–1057

[44] Xie H, Li X, Fang Z, Wang Y, Li Q, Shi L, Bai B, Wei N, Hou Z (2014) Carbon geological utilization and storage in China: current status and perspectives. Acta Geotech 9(1):7–27